External Inverse-compton and Proton Synchrotron Emission from the Reverse Shock as the Origin of VHE Gamma Rays from the Hyper-bright GRB 221009A

B. Theodore Zhang (张兵)[1] , Kohta Murase[1,2,3,4,5] , Kunihito Ioka[1] , Deheng Song[1] , Chengchao Yuan (袁成超)[6] , and Péter Mészáros[2,3,4]

[1] Center for Gravitational Physics and Quantum Information, Yukawa Institute for Theoretical Physics, Kyoto University, Kyoto, Kyoto 606-8502, Japan; bing.zhang@yukawa.kyoto-u.ac.jp
[2] Department of Physics, The Pennsylvania State University, University Park, PA 16802, USA
[3] Department of Astronomy and Astrophysics, The Pennsylvania State University, University Park, PA 16802, USA
[4] Center for Multimessenger Astrophysics, Institute for Gravitation and the Cosmos, The Pennsylvania State University, University Park, PA 16802, USA
[5] School of Natural Sciences, Institute for Advanced Study, Princeton, NJ 08540, USA
[6] Deutsches Elektronen-Synchrotron DESY, Platanenallee 6, D-15738 Zeuthen, Germany
Received 2022 November 23; revised 2023 March 16; accepted 2023 March 24; published 2023 April 17

Abstract

The detection of the hyper-bright gamma-ray burst (GRB) 221009A enables us to explore the nature of the GRB emission and the origin of very high-energy gamma rays. We analyze the Fermi Large Area Telescope (Fermi-LAT) data of this burst and investigate the GeV–TeV emission in the framework of the external reverse-shock model. We show that the early ∼1–10 GeV emission can be explained by the external inverse-Compton mechanism via upscattering MeV gamma rays by electrons accelerated at the reverse shock, in addition to the synchrotron self-Compton component. The predicted early optical flux could have been brighter than that of the naked-eye GRB 080319B. We also show that proton synchrotron emission from accelerated ultrahigh-energy cosmic rays (UHECRs) is detectable and could potentially explain ≳TeV photons detected by LHAASO or constrain the UHECR acceleration mechanism. Our model suggests that the detection of $\mathcal{O}(10\,\mathrm{TeV})$ photons with energies up to ∼18 TeV is possible for reasonable models of the extragalactic background light without invoking new physics and predicts anticorrelations between MeV photons and TeV photons, which can be tested with the LHAASO data.

Unified Astronomy Thesaurus concepts: Gamma-ray bursts (629); Gamma-ray astronomy (628); Gamma-ray sources (633); High energy astrophysics (739); Relativistic jets (1390); Non-thermal radiation sources (1119)

1. Introduction

Gamma-ray bursts (GRBs) are among the most luminous explosions in the universe (Mészáros 2006; Kumar & Zhang 2014). In 2019, the detection of two TeV bursts, GRB 190114C (MAGIC Collaboration et al. 2019; MAGIC Collaboration 2019) and GRB 180720B (Abdalla et al. 2019), opened a new window in the very high-energy (VHE) (≳0.1 TeV) band for studying GRBs, providing us with new opportunities to investigate the nature of GRBs (see Gill & Granot 2022 and Miceli & Nava 2022 for reviews).

On 2022 October 9, GRB 221009A was triggered by the Fermi Gamma-Ray Burst Monitor (GBM) at $T_0 = 13{:}16{:}59.99$ UT (Veres et al. 2022). The Swift Burst Alert Telescope also triggered GRB 221009A around 1 hr later (Dichiara et al. 2022). GRB 221009A is an extraordinarily bright and energetic GRB with isotropic-equivalent energy $\mathcal{E}_k \sim 3 \times 10^{55}$ erg for a radiative efficiency of 10% (Frederiks et al. 2022) at a redshift $z = 0.15$ (de Ugarte Postigo et al. 2022). The Fermi Large Area Telescope (Fermi-LAT) reported the detection of >100 MeV gamma rays with maximum photon energy reaching 99.3 GeV (Pillera et al. 2022). Remarkably, it was reported by the Large High Altitude Air Shower Observatory (LHAASO) that more than 5000 gamma rays with energy beyond 500 GeV from

GRB 221009A were detected, and the highest-energy gamma-ray energy reaches 18 TeV (Huang et al. 2022).

The production of VHE gamma rays from GRBs up to ∼TeV has been widely discussed in the standard afterglow model via the synchrotron self-Compton (SSC) process (e.g., Mészáros & Rees 1994; Dermer et al. 2000; Sari & Esin 2001; Zhang & Mészáros 2001; Ren et al. 2022) or the external inverse-Compton (EIC) process (e.g., Wang et al. 2006; Murase et al. 2010, 2011; Toma et al. 2011; He et al. 2012; Veres & Mészáros 2014; Kimura et al. 2019; Zhang et al. 2021a, 2021b). Proton synchrotron emission has been proposed as one alternative mechanism to generate VHE gamma rays from GRBs (e.g., Totani 1998; Zhang & Mészáros 2001; Murase et al. 2008; Asano et al. 2009; Isravel et al. 2022), which usually requires protons to be accelerated to the ultrahigh-energy (UHE) range. The proton synchrotron emission has an advantage in the generation of ≳10 TeV gamma rays, which is usually difficult for SSC and EIC processes due to the limitation of the Klein–Nishina effect. Motivated by the detection of $\mathcal{O}(10\,\mathrm{TeV})$ gamma rays from GRB 221009A by the LHAASO observatory, we study the proton synchrotron radiation process of GRB 221009A in detail.

It has been proposed that the acceleration of ultrahigh-energy cosmic rays (UHECRs) is possible in the internal shock model (e.g., Waxman 1995; Vietri 1996) or reverse-shock (RS) model of GRBs (e.g., Waxman & Bahcall 2000; Murase 2007; Murase et al. 2008; Zhang et al. 2018), while the acceleration of UHECRs in the forward-shock (FS) region via the diffusive shock acceleration mechanism is difficult due to the low

magnetic field strength of the external medium (Gallant & Achterberg 1999; Murase et al. 2008; Sironi et al. 2015). GRB internal shocks may occur at much smaller radii, where the escape of $\mathcal{O}(10\,\mathrm{TeV})$ gamma rays is difficult unless the Lorentz factor is extremely large (e.g., Murase et al. 2022). One of the possibilities is the UHECR proton synchrotron emission process in the RS model. The observed prompt emission in the MeV band indicates that GRB 221009A is a long-lasting GRB with T_{90} of at least ~ 600 s, implying a thick ejecta shell case where the long-lasting RS can be expected. Also, during the early phase of the RS, the extraordinarily bright prompt photons can be upscattered by the high-energy electrons accelerated in the reverse-shock region to produce high-energy gamma rays that may be related to Fermi-LAT observations (e.g., Beloborodov 2005).

Throughout this work, we use $Q = Q_x 10^x$ in centimetre–gram–second system units.

2. GeV–TeV Gamma Rays from a Reverse-shock Model

We analyze the Fermi-LAT data collected between 203 and 1000 s after the Fermi GBM trigger time of $T_0 = 13{:}16{:}59.99$ UT (Pillera et al. 2022; Veres et al. 2022). Our region of interest (ROI) is a $10°$ by $10°$ region centered around the location of the GRB as reported by Pillera et al. (2022; R. A. $= 288°.28$, decl. $= 19°.49$). We select the events from the P8R3_TRANSIENT020 class with energies between 0.1 GeV and 10 GeV. We consider three time intervals after T_0: 203–294 s, 294–410 s, and 410–1000 s. In each time interval, we perform unbinned likelihood analysis by varying a point source placed at the center of the ROI. We also include the Galactic interstellar emission model gll_iem_v07.fits and the isotropic diffuse emission model iso_P8R3_TRAN-SIENT020_V3_v1.txt, and their normalizations are allowed to vary freely. The first time interval overlaps with the LAT Bad Time Interval due to photon pileup (Omodei et al. 2022a, 2022b). We only include it for reference purposes. The LAT photons were detected in the time interval $T_0 + 294$ s to $T_0 + 410$ s, and the integrated photon flux between 0.1 GeV and 10 GeV is $(4.0 \pm 0.4) \times 10^{-3}$ ph cm^{-2} s^{-1} with a photon index of 1.76 ± 0.09. We do not find photons from the direction of the GRB during the time interval $T_0 + 410$ s to $T_0 + 1000$ s. The 95% upper limit of the flux is 3.5×10^{-3} ph cm^{-2} s^{-1}. The flux light curve is shown in Figure 1.

In Figure 1, we also show the peak time of the observed pulse of GRB prompt emission detected by Konus-Wind at 13:17:01.648 UT (Frederiks et al. 2022). We can see there was active prompt emission during the Fermi-LAT observations within the time interval $T - T_0 \sim 200\text{–}400$ s, while the prompt emission becomes weaker at later times up to ~ 600 s, which may also be regarded as the flare phase (Frederiks et al. 2023; An et al. 2023). Considering the long-lasting prompt emission of GRB 221009A, in this work, we assume that the GRB ejecta is thick with duration time 600 s (e.g., Ioka et al. 2005).

We consider two episodes, where the first episode (Episode I) is strongly affected by the active prompt emission phase, while the second episode (Episode II) is much less affected by the prompt emission until the RS finishes crossing the ejecta. However, the detailed modeling of the dynamical evolution of the RS can be complicated (Sari & Piran 1995; Sari 1997). For the purpose of this work, we analytically derive the characteristic radius and time of the RS at the shock crossing
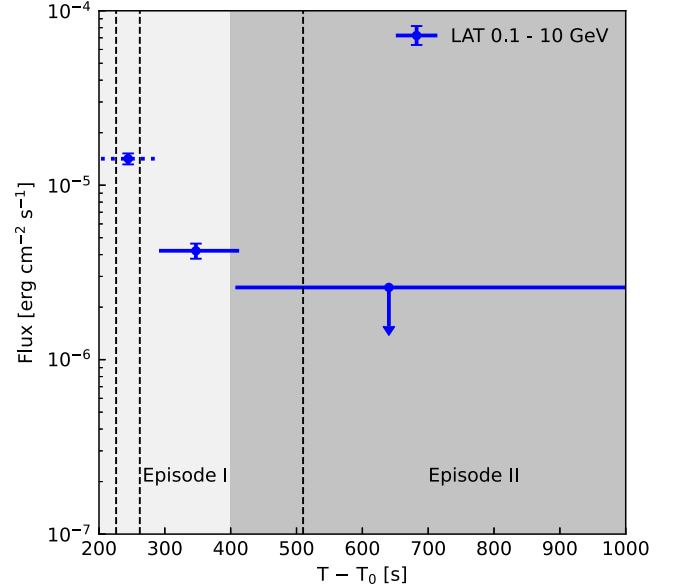
Figure 1. The flux light curve observed by the Fermi-LAT between $T_0 + 203$ s and $T_0 + 1000$ s. The first time interval overlaps with the LAT Bad Time Interval due to photon pileup and therefore is only included for reference purposes. The black dashed lines indicate the three peak times of the prompt emission observed by the Konus-Wind.

time $t_\times$ (Panaitescu & Kumar 2004; Murase 2007), where the RS finishes crossing the ejecta.

When the ultrarelativistic thick ejecta propagates into the external medium, two types of shocks are formed: an RS, which propagates back into the ejecta shell, increasing the internal energy; and an FS), which propagates into the external medium and energizes the swept-up matter. The typical crossing time $t_\times$ for the RS to complete its crossing through the ejecta depends on the width of the ultrarelativistic ejecta shell Δ that represents the geometrical thickness measured in the stellar frame. In the thick ejecta shell regime, the ejecta width can be estimated as $\Delta \approx c\delta T \simeq 1.9 \times 10^{13}\, \delta T_{2.8}$ cm, where δT is the duration of the GRB ejecta released by their source measured in the GRB frame. Then the crossing radius of the RS is $r_\times \simeq 3.8 \times 10^{17}\, \mathcal{E}_{k,55}^{1/4} n^{-1/4} \delta T_{2.8}^{1/4}$ cm where $\mathcal{E}_k$ is the isotropic-equivalent kinetic energy and n is the constant density of the external medium. The crossing time is $t_\times(\delta T) \approx 0.71\delta T(1+z) \simeq 540\delta T_{2.8}$ s, and hereafter the dependence on z is neglected for simplicity. The Lorentz factor of the shocked ejecta at the crossing radii $r_\times$ can be written as $\Gamma_\times \simeq 83\, \mathcal{E}_{k,55}^{1/8} n^{-1/8} \delta T_{2.8}^{-3/8}$ and $\Gamma_{\rm rel} \approx 0.5(\Gamma_\times / \Gamma_0 + \Gamma_0/\Gamma_\times) \simeq 1.7\Gamma_{0,2.4}$ when measured in the stellar frame and in the frame of unshocked ejecta, respectively. Here Γ_0 is the initial Lorentz factor of GRB ejecta. The RS is relativistic before it crosses the shell. The contribution to the shell width due to the velocity spread can be estimated as $r_\times/2\Gamma_0^2 \simeq 3.1 \times 10^{12}\, \mathcal{E}_{k,55}^{1/4} n^{-1/4} \delta T_{2.8}^{1/4} \Gamma_{0,2.4}^{-2}$ cm $< \Delta$ as expected in the thick ejecta shell regime (Sari & Piran 1995).

For the earlier evolution phase of the RS, especially for Episode I, we assume that only a fraction of the total ejecta energy $\mathcal{E}_{k,\mathrm{I}} \approx (\delta T_{\mathrm{I}}/\delta T)\mathcal{E}_k$ carried by the outer edge of the ejecta shell is transferred to the external medium during $t_{\times,\mathrm{I}} \equiv t_\times(\delta T_{\mathrm{I}}) < t_\times$. Thus, we can use the same method as above to estimate the characteristic radius and Lorentz factor of the shocked ejecta after the RS crosses. For Episode II, we

Table 1
Physical Parameters Used in the RS Model

| Parameter	Episode I	Episode II
Γ_0	250	250
$\mathcal{E}_k$[a] [erg]	2×10^{55}	2×10^{55}
$n_{\rm ex}$ [cm^{-3}]	1	1
δT [s]	300[b]	600
ϵ_B	0.05	0.5
ϵ_e	0.35	0.02
f_e	0.8	0.01
s_e	2.6	2.6
ϵ_p	0.1	0.08
s_p	2.0	2.0
$L_{\rm GRB\gamma}^{\rm iso}$ [erg s^{-1}]	2×10^{52}	2×10^{50}

Notes.
[a] The dissipated energy during Episode I is only a fraction of the total kinetic energy $\mathcal{E}_{k,\rm I} \approx (\delta T_{\rm I}/\delta T)\mathcal{E}_k$ as explained in Section 2 of the main text. For Episode II, we have $\mathcal{E}_{k,\rm II} \approx \mathcal{E}_k$.
[b] This is the duration of the GRB ejecta during Episode I $\delta T_{\rm I}$.

adopt the same assumptions and use the same method, except that $\delta T_{\rm II} \sim \delta T$ and $\mathcal{E}_{k,\rm II} \sim \mathcal{E}_k$.

Now we proceed to derive the emission properties of the shocked ejecta at the shock crossing radius for both episodes. Note that for Episode I, the physical quantities in the following equations are normalized to the numerical values closer to those expected for Episode II. For Episode II, the magnetic field strength in the comoving frame is estimated as $B_\times = [32\pi\epsilon_B n_{\rm ej} m_p c^2 (\Gamma_{\rm rel} - 1)\ (\Gamma_{\rm rel} + 3/4)]^{1/2} \simeq 8.6\ {\rm G} \epsilon_{B,-1}^{1/2} \mathcal{E}_{k,55}^{1/4} \Gamma_{0,2.4}^{-1} \delta T_{2.8}^{-3/4} n^{1/4}\ (g(\Gamma_{\rm rel})/1.7)^{1/2}$, where ϵ_B is the energy fraction of internal energy that is converted into magnetic energy, the proton number density of the unshocked ejecta is $(n_{\rm ej} \simeq 3.2 \times 10^3\ \mathcal{E}_{k,55}^{1/2} \Gamma_{0,2.4}^{-2} \delta T_{2.8}^{-3/2} n^{1/2}\ {\rm cm}^{-3}$, and $g(\Gamma_{\rm rel}) \equiv (\Gamma_{\rm rel} - 1)(\Gamma_{\rm rel} + 3/4)$. The total number of electrons energized by the RS is $N_e^r = \mathcal{E}_k/\Gamma_0 m_p c^2 \simeq 2.8 \times 10^{55}\ \mathcal{E}_{k,55}\Gamma_{0,2.4}^{-1}$. The minimum electron Lorentz factor after shock acceleration can be estimated as $\gamma_m \approx (\epsilon_e/f_e)[(s_e - 2)/(s_e - 1)](m_p/m_e)(\Gamma_{\rm rel} - 1) \simeq 4.2 \times 10^2$ $\epsilon_{e,-}f_{e,-1}^{-1}$ for $s_e = 2.6$ and $\Gamma_{\rm rel} = 1.7$, where the energy fraction ϵ_e of the post-shock internal energy is converted into electron nonthermal energy, f_e is the number fraction of accelerated electrons, and s_e is the electron spectral index. The main difference between the treatment of Episode I and Episode II are the values adopted for ϵ_B and ϵ_e (see Table 1). We then derive the steady-state electron energy distribution considering various cooling processes, including adiabatic cooling, synchrotron cooling, SSC cooling, and EIC cooling, using the iteration method described in Murase et al. (2011) and Zhang et al. (2021a). The comoving frame nonthermal proton energy density is determined by $U_p \approx \epsilon_p \mathcal{E}_k/(4\pi r_\times^2 \Gamma_\times^2 \Delta)$, where ϵ_p is the fraction of downstream energy transferred to the nonthermal protons. The comoving frame minimum proton energy is $\varepsilon_{p,\rm min} \approx \Gamma_{\rm rel} m_p c^2$. The maximum proton energy achieved under the confinement condition $t_{\rm acc} < t_{\rm dyn}$ is $E_{\rm max,dyn} \approx \eta^{-1} e B_\times r_\times \simeq 1.0 \times 10^{21}\ {\rm eV}\ \eta^{-1}$ $\mathcal{E}_{k,55}^{1/2}\Gamma_{0,2.4}^{-1}\delta T_{2.8}^{-1/2}\epsilon_{B,-1}^{1/2}(g(\Gamma_{\rm rel})/1.7)^{1/2}$. Here, we define the acceleration timescale as $t_{\rm acc} = \eta t_L$, where t_L is the Larmor time and η is a coefficient. Note η is $\sim$a few in the Bohm limit (e.g., Sironi et al. 2015). The production of UHECRs at the GRB RS is possible (e.g., Murase et al. 2008; Zhang et al.
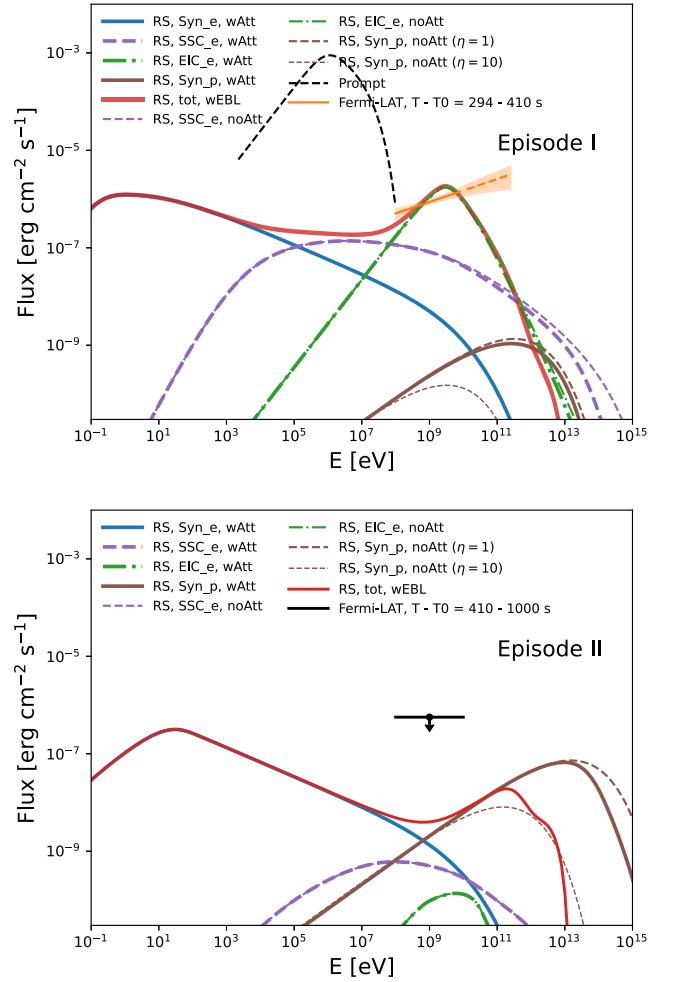
Figure 2. Multiwavelength energy spectra up to the VHE energy range in our RS model in Episode I (upper panel) and Episode II (lower panel), respectively. The black dashed line in the upper panel is the prompt spectrum with an exponential cutoff at $E_{\gamma,\rm max} = 20$ MeV. The orange line in the upper panel indicates the averaged energy spectrum observed by Fermi-LAT within $T - T_0 = 294$–410 s, extrapolated to the energy of 300 GeV. The black line in the low panel is the Fermi-LAT 95% upper limits within $T - T_0 = 410$–1000 s.

2018), where the maximum proton energy can be limited by various cooling processes, e.g., for synchrotron cooling we have $E_{\rm max,syn} \simeq 5.5 \times 10^{20}\ {\rm eV}\ Z^{-3/2}\eta^{-1/2}$ $\epsilon_{B,-1}^{-1/4}\Gamma_{0,2.4}^{1/2}n^{-1/4}(g(\Gamma_{\rm rel})/1.7)^{-1/4}$. We also include the effect of photomeson cooling on the maximum energy of protons, which depends on the energy density of the target photon fields. The effect of overlapping of the prompt emission in the reverse-shocked region is considered, where the comoving prompt photon energy density measured in the reverse-shocked region is $U_{\rm GRB\gamma} \approx L_{\rm GRB\gamma}^{\rm iso}/4\pi r_\times^2 \Gamma_\times^2 c$. The Band function is used for modeling the energy spectra of the prompt emission, where the low-energy power-law index is $\alpha = 1.1$, the high-energy power-law index is $\beta = 2.6$, and the observed peak energy is $E_{\rm pk} = 1$ MeV (Frederiks et al. 2022).

3. Results

The predicted multiwavelength energy spectra for the two episodes are shown in Figure 2, where the corresponding parameters are summarized in Table 1.

3.1. Episode I—Upscattered Prompt Emission?

In the upper panel of Figure 2, we show the multiwavelength energy spectrum from various processes for Episode I. The orange shaded region represents the average energy spectrum observed by Fermi-LAT within $T - T_0 = 294\text{–}410$ s,[7] extrapolated to 300 GeV. The dotted–dashed curve is the upscattered prompt emission by the nonthermal electrons accelerated in the RS region in Episode I, which dominates energy flux beyond ~ 1 GeV, while the dashed curve is the SSC component, which dominates the energy flux from 0.1 to 1 GeV. The synchrotron component is indicated by the blue solid curve, while the proton synchrotron component is marked as the brown solid curve. We also overlay the prompt emission, assuming Band function with an exponential cutoff at $E_{\gamma,\max} = 20$ MeV. The corresponding parameters are summarized in Table 1.

At Episode I, the microphysical parameters satisfy $\epsilon_e > \epsilon_B$, and the inverse-Compton component dominates the gamma-ray emission. We find that the EIC spectra can explain the hard energy spectrum observed by Fermi-LAT above ~ 1 GeV. Note that the detected ~ 99.3 GeV photon by Fermi-LAT at $T - T_0 = 240$ s may be explained by the EIC component, considering the enhancement of the prompt photons during the first time interval mentioned in Figure 1. However, the proton synchrotron component is not important in Episode I because the dominance of prompt MeV gamma rays in the energy density limits the emission power of the synchrotron component. We note that the predicted early optical flux could have been brighter than that of the naked-eye GRB 080319B (Racusin et al. 2008).

3.2. Episode II—Proton Synchrotron Emission?

In the lower panel of Figure 2, we show the energy spectrum from various processes for Episode II. Due to the decrease of the prompt luminosity by at least 2 orders of magnitude, the EIC component is no longer important, while the proton synchrotron emission is more prominent at Episode II given that the magnetic fields are strong. As shown in Table 1, we assume that the microphysical parameter $\epsilon_B = 0.5$ is larger than the value adopted in Episode I. Such a change of ϵ_B is possible for long-lasting magnetic energy-dominated GRB ejecta. Initially, the value of ϵ_B is very high for magnetic energy-dominated GRB ejecta. During Episode I, most of the GRB ejecta energy is released in the form of the extraordinarily strong prompt emission pulse with abundant pair production, which may effectively suppress ϵ_B, especially if the prompt gamma rays are produced by magnetic dissipation and the RS is stronger due to the weak magnetic energy in the GRB ejecta. Thus, we could expect strong inverse-Compton emission at Episode I. Later, the RS continues to cross the inner region of the GRB ejecta, which is still magnetic energy dominated, and it becomes weak, consistent with the observations. We can expect higher values of ϵ_B in Episode II, and the proton synchrotron emission is very efficient. The above physical process could also explain the decrease of ϵ_e and ϵ_p in Episode II.

The peak energy from proton synchrotron emission can reach ~ 10 TeV without extragalactic background light (EBL) absorption. Remarkably, the corresponding spectral index of
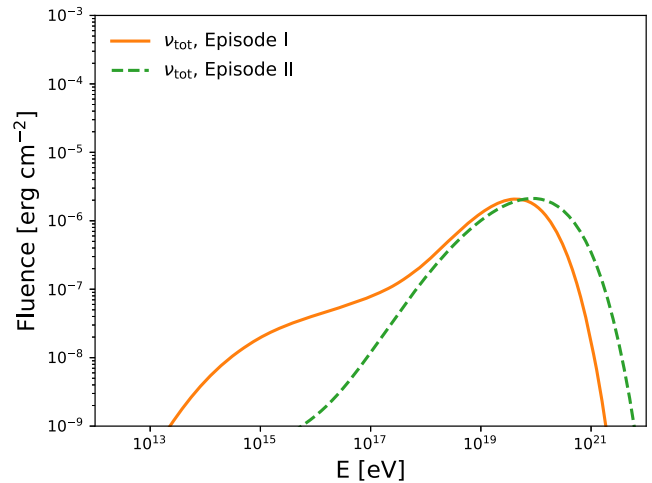

Figure 3. Neutrino fluences emitted during the time window 100 s (Episode I) and 300 s (Episode II).

the energy flux from proton synchrotron emission is $(3 - s_p)/2 = 1/2$ for $s_p = 2$, which is larger than the spectral index ~ 0.2 inferred from Fermi-LAT observations in Episode I. The harder spectral index enhances the fraction of $\mathcal{O}(10 \text{ TeV})$ photons in the total observed gamma rays even though it is undergoing EBL-induced attenuation during the propagation from the source to Earth (e.g., Baktash et al. 2022; Zhao et al. 2022).

3.3. High-energy Neutrino Production

In Figure 3, we show the predicted neutrino fluences from Episode I and Episode II, respectively. The physical parameters used for the corresponding calculations are identical to those in Table 1. The neutrino energy spectrum predicted in Episode I has two bumps, where the low-energy bump with peak energy at $\sim$ PeV energy range is due to the photomeson production interaction between high-energy protons with prompt target photon fields, while the high-energy bump with peak energy at ~ 10 EeV is the result between the interaction of UHE protons with the lower-energy synchrotron photons from the RS. The neutrino energy spectrum predicted in Episode II only shows one bump, which is consistent with the assumption that the effect of prompt emission is no longer important in Episode II. The maximum proton energy is also higher in Episode II due to the strong magnetic fields, which is consistent with the neutrino spectrum where the neutrino has higher energy in Episode II. Note that the cooling of secondary muons and pions is neglected when calculating the neutrino flux in our model, which will reduce the flux of the higher-energy part of the observed neutrino spectrum, especially for Episode II (Murase 2007). The predicted neutrino fluence is consistent with the upper limits reported by IceCube (Ai & Gao 2022; Murase et al. 2022; Abbasi et al. 2023).

4. Discussion and Implications

4.1. Anticorrelation

The $\gamma\gamma$ optical depth $\tau_{\gamma\gamma}$ due to the interaction with prompt photons at the shocked ejecta region can be estimated with the

---

7 We do not consider gamma rays detected in the first time interval $T - T_0 = 203\text{–}294$ s, which overlaps with the LAT Bad Time Interval.

following formula (e.g., Murase et al. 2022),

$$
\tau_{\gamma\gamma}^{\text{prompt}}
\simeq 11 \frac{\eta_{\gamma\gamma,-1} L_{\text{GRB}\gamma,53.5}^{\text{iso}}}{r_{17.3}\Gamma_{\times,2}^2 E_{\text{pk,MeV}}}
\begin{cases}
(E_\gamma/\tilde{E}_{\gamma,b})^{\beta-1}, & E_\gamma < \tilde{E}_{\gamma,b}, \\
(E_\gamma/\tilde{E}_{\gamma,b})^{\alpha-1}, & E_\gamma > \tilde{E}_{\gamma,b},
\end{cases}
\tag{1}
$$

where $\eta_{\gamma\gamma} \sim 0.1$ (Svensson 1987), $\tilde{E}_{\gamma,b} \approx \Gamma_\times^2 m_e^2 c^4 / E_{\text{pk,MeV}} \simeq 2.6\ \Gamma_{\times,2}^2$ GeV represents the typical energy of high-energy gamma rays that interact with target photons of peak energy $E_{\text{pk,MeV}}$ in the observer frame, and $L_{\text{GRB}\gamma}^{\text{iso}}$ represents the isotropic-equivalent luminosity in the Konus-Wind band where the bolometric correction has been accounted for. The optical depth at 1 TeV is $\tau_{\gamma\gamma}(1\ \text{TeV}) \sim 20$ for $\alpha = 1.1$. In addition, the synchrotron photons become dominant in the energy range below $\lesssim$ keV in Episode I compared to the prompt target photons as shown in Figure 2. Then the optical depth can be estimated as

$$
\tau_{\gamma\gamma}^{\text{syn}} \simeq 2300 \frac{\eta_{\gamma\gamma,-1} L_{\gamma,50}^{\text{syn}}}{r_{17.3}\Gamma_{\times,2}^2 E_{\gamma,m}^{\text{syn}}}
$$
$$
\times
\begin{cases}
(E_\gamma/\tilde{E}_{\gamma,m})^{\frac{s_e}{2}}, & E_\gamma < \tilde{E}_{\gamma,m} \\
(E_\gamma/\tilde{E}_{\gamma,m})^{\frac{1}{2}}, & \tilde{E}_{\gamma,c} > E_\gamma > \tilde{E}_{\gamma,m},
\end{cases}
\tag{2}
$$

where L_γ^{syn} is the luminosity of synchrotron emission at the synchrotron peak energy of the RS component, $E_{\gamma,m}^{\text{syn}} \simeq 1$ eV ($E_{\gamma,c}^{\text{syn}} \simeq 0.1$ eV) is the observed synchrotron peak (cooling) energy in the fast cooling regime, $\tilde{E}_{\gamma,m} \approx \Gamma_\times^2 m_e^2 c^4 / E_{\gamma,m}^{\text{syn}} \simeq 2600\ \Gamma_{\times,2}^2$ TeV and $\tilde{E}_{\gamma,c} \approx \Gamma_\times^2 m_e^2 c^4 / E_{\gamma,c}^{\text{syn}} \simeq 26000\ \Gamma_{\times,2}^2$ TeV are the typical energies of high-energy gamma rays that interact with target photons with energy $E_{\gamma,m}^{\text{syn}}$ and $E_{\gamma,c}^{\text{syn}}$ Then the optical depth at 10 TeV is $\tau_{\gamma\gamma}(10\ \text{TeV}) \sim 2$ for $s_e = 2.6$. Note that the analytical calculation of the optical depth in Equation (2) is only valid for $E_\gamma < \tilde{E}_{\gamma,c}$ as the differential spectral index drops below unity ($2/3 < 1$) when the photon energy is below $E_{\gamma,c}^{\text{syn}}$. Thus, in our model, we predict the anticorrelation of the $\gtrsim$ TeV photons during the strongest prompt GRB emission phase, with the former escaping at later times. For Episode II, due to the lower luminosity of prompt emission and the synchrotron photons, we can expect the escape of $\gtrsim$ TeV photons simultaneously with low-energy photons.

4.2. Implications for LHAASO Detection

In Figure 4, we show the number of photons predicted in our model that can be detected by LHAASO. Considering the uncertainties on the measured EBL models, we adopt three representative EBL models, namely *Franceschini08* (Franceschini et al. 2008), *Gilmore12* (Gilmore et al. 2012), and *Finke10* (Finke et al. 2010). We adopt the effective area of the LHAASO-WCDA for photons provided in Wang et al. (2022) for zenith window $15° < \theta < 30°$ and the effective area from LHAASO-KM2A (Ma et al. 2022). The integrated number of events can be estimated as

$$
N(>E) = \int_E^{E_{\text{max}}} dE\, F(E) A_{\text{eff}}^\gamma(E,\theta)\Delta T,
\tag{3}
$$
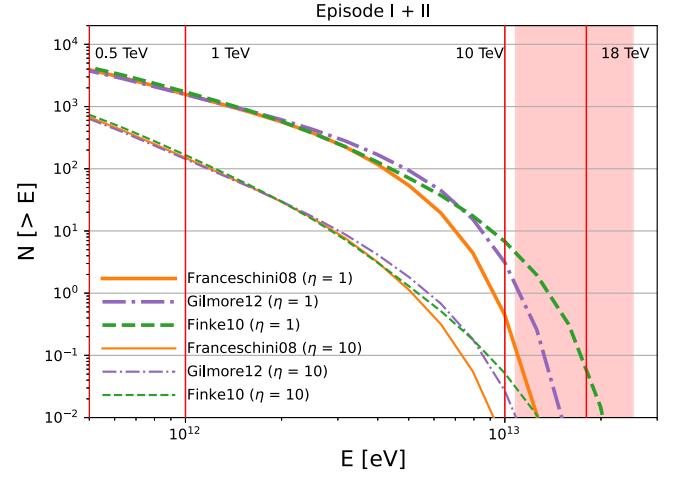
Figure 4. The predicted detection (cumulative) number for the LHAASO detector with the energy spectrum predicted from our model using three different EBL models with the total integration time $\Delta T = 100$ s for Episode I and $\Delta T = 300$ s for Episode II. The vertical lines indicate the observed photon energy, and the shaded region corresponds to the energy range $18 \times (100\% \pm 40\%)$ TeV with a $\sim 40\%$ energy resolution at the 18 TeV energy band of LHAASO-KM2A (Ma et al. 2022).

where $F(E)$ is the predicted energy spectrum, $A_{\text{eff}}^\gamma(E,\theta)$ is the effective area including both LHAASO-WCDA and LHAASO-KM2A, and ΔT is the integration time. Even though the LHAASO-WCDA dominates the effective area at low energy, the effective area of LHAASO-KM2A is comparable to LHAASO-WCDA above ~ 10 TeV (Ma et al. 2022). If we adopt a typical integration time 300 s for Episode II, then the number of photons detected is $N(> 0.5\ \text{TeV}) \sim 4000$ for photons with energy larger than 500 GeV, $N(> 1\ \text{TeV}) \sim 1500$ for photons with energy larger than 1 TeV, and $N(> 10\ \text{TeV}) \sim 7$ for photons with energy larger than 10 TeV. The expected cosmic-ray background for LHAASO-WCDA can be estimated with the same method used in Wang et al. (2022). We find that the photons with energies larger than 500 GeV (1 TeV) could be detected with LHAASO-WCDA with a significance level ~ 25 standard deviation (~ 15 s. d.) estimated through Equation (17) of Li & Ma (1983) using the fitted cosmic-ray spectrum in Particle Data Group et al. (2020).

Even though we expect $N(> 0.5\ \text{TeV}) \lesssim 300$ photons to be detected in Episode I, the detection of photons with energy above 1 TeV may be challenging for LHAASO-WCDA in Episode I, where the significance level is expected to be less than ~ 2 s. d. in our fiducial case. TeV photons during Episode I mainly come from the SSC emission in our model. However, there is significant uncertainty in the SSC component, and if more $\gtrsim$ TeV gamma rays have been detected by LHAASO in Episode I, it would indicate that the SSC component becomes more important than the fiducial case shown in this work or the proton synchrotron emission is enhanced because of the larger value of ϵ_B as in the case of Episode II. The VHE gamma rays detected by LHAASO in Episode I may be primarily contributed by the SSC component resulting from nonthermal electrons that are accelerated by the FS (e.g., Ren et al. 2022; Sato et al. 2023). The fitting of the low-frequency radio to optical spectra at the earlier stages indicates that additional components, possibly resulting from synchrotron emission from ejecta swept by the RS, are required beyond the standard

FS model (O'Connor et al. 2023). However, further investigation using multiwavelength data is needed to determine the relative contribution of the observed VHE gamma rays from FS and RS.

In the thick-shell case, it takes time for the shocked ejecta to get adjusted to the Blandford–McKee profile after the RS crosses the ejecta. As in synchrotron emission from primary electrons accelerated at the RS (Kobayashi 2000), we expect that the proton synchrotron light curve will decay with a temporal index of $-(73s_p + 21)/96 \sim -1.7$ for $s_p = 2$, which is typically steeper than the FS case. However, the details of the RS light curve depend on the profile of the ejecta, for long-lasting RSs especially from $t_{\times,\mathrm{I}}$ to $t_\times$, which can be shallower than the standard case.

The LHAASO-KM2A is extremely effective for suppressing the cosmic-ray background (Ma et al. 2022), so the detection of dozens of photons with energy $\mathcal{O}(10\,\mathrm{TeV})$ is reasonable considering the energy resolution. The energy resolution at $\mathcal{O}(10\,\mathrm{TeV})$ is $\Delta E/E \sim 45\%$ for LHAASO-KM2A and $\Delta E/E \sim 60\%$ for LHAASO-WCDA. Our results indicate that even without considering the effect of new physics on the propagation of VHE gamma rays, e.g., photon mixing with axion-like particles (Baktash et al. 2022; Galanti et al. 2022; Nakagawa et al. 2023; Troitsky 2022) and Lorentz invariance violation (Finke & Razzaque 2022; Li & Ma 2022; Zhu & Ma 2022), the detection of ~ 18 TeV photons by LHAASO-KM2A can be explained for reasonable EBL models. Another possible explanation for the detection of ~ 18 TeV is the intergalactic electromagnetic cascade due to the propagation of UHECRs (Batista 2022; Das & Razzaque 2022; Mirabal 2022). Both models also require the efficient production of UHECRs from GRBs. But in the intergalactic cascade scenario, the time delay of the photon arrival during the propagation of UHECRs and the development of the electromagnetic cascade depends strongly on the magnetic field structure of the host galaxy, the host galaxy cluster, and the intergalactic medium, and the time delay is longer given that the magnetic field strength is larger than $10^{-17}\,\mathrm{G}$ (Takahashi et al. 2008; Murase et al. 2009, 2012; Mirabal 2022).

The default value of the coefficient in the acceleration timescale formula $t_{\mathrm{acc}} = \eta t_L$ is set to $\eta = 1$, which may be optimistic. If we adopt a more considerable value of $\eta = 10$, then the proton synchrotron component would be reduced, which makes the detection of $\gtrsim$TeV gamma rays more challenging in Episode II as shown in Figure 4. Thus, our results imply that the RS of the long-lasting GRB 221009A should be a very efficient accelerator of nonthermal particles. If most of the $\gtrsim$TeV gamma rays are detected after Episode II, which is $T \sim 600$ s in this work, then this would mean that the GRB ejecta duration is a bit longer and the RS finishes crossing the GRB ejecta at later times.

5. Summary

The detection of GRB 221009A in the VHE gamma-ray band up to $\mathcal{O}(10\,\mathrm{TeV})$ by LHAASO provides us with an opportunity to study the radiative processes of GRBs in the highest energy range. In this work, we studied the origin of VHE gamma rays from GRB 221009A in the framework of the RS model where nonthermal electrons and protons are expected to be accelerated. The RS could last up to thousands of seconds after the start of GRB, which is consistent with the long-lasting prompt emission observed from GRB 221009A.

We considered two episodes, where the emission from the RS in the first episode (Episode I) is strongly affected by the strong prompt emission, while the effect of prompt emission becomes weak in the second episode (Episode II). In addition, the microphysical parameters, e.g., ϵ_B and ϵ_e, could be different from Episode I to Episode II, causing different behavior in the emission processes.

Our results show that the upscattered prompt MeV photons by the nonthermal electrons accelerated in the RS region in Episode I mainly contribute to the energy flux observed by Fermi-LAT above $\sim$GeV, in addition to the SSC component. The emission from the proton synchrotron process is not important in Episode I because of the presence of MeV gamma rays and weak magnetic field strength.

We found that the proton synchrotron process can dominate the output in the VHE band in Episode II, where the magnetic field strength is strong enough to increase the proton synchrotron emission significantly. Our rough estimates show that ~ 4000 photons with energy larger than 0.5 TeV can be detected by LHAASO in Episodes I and II, which may be consistent with the number of photons detected by LHAASO within 2000 s. Due to the hard spectral index of the proton synchrotron emission compared to the inverse-Compton process as inferred from Fermi-LAT data, it is plausible to detect dozens of $\mathcal{O}(10\,\mathrm{TeV})$ photons using reasonable EBL models without invoking new physics.

Note that the FS has a similar energy to the RS, and it may also contribute to the VHE emission. The FS could enhance the number of $\sim$ TeV gamma rays detected by LHAASO, but it is difficult for $\mathcal{O}(10\,\mathrm{TeV})$ gamma rays to be detected, which emphasizes the role of proton synchrotron emission from the RS as proposed in this work.

In the future, we can expect more GRBs to be detected in the VHE gamma-ray band, especially with the Cherenkov Telescope Array (Kakuwa et al. 2012; Inoue et al. 2013). Our work suggests that the observation of GRB in the VHE gamma-ray band can be used for constraining the particle acceleration and radiative processes of nonthermal electrons and protons in the RS model.

ORCID iDs

B. Theodore Zhang
(张兵) ⓘ https://orcid.org/0000-0003-2478-333X
Kohta Murase ⓘ https://orcid.org/0000-0002-5358-5642
Kunihito Ioka ⓘ https://orcid.org/0000-0002-3517-1956
Deheng Song ⓘ https://orcid.org/0000-0003-3441-4212
Chengchao Yuan
(袁成超) ⓘ https://orcid.org/0000-0003-0327-6136
Péter Mészáros ⓘ https://orcid.org/0000-0002-4132-1746

References

Abdalla, H., Adam, R., Aharonian, F., et al. 2019, Natur, 575, 464
Ai, S., & Gao, H. 2023, ApJ, 944, 115
An, Z.-H., Antier, S., Bi, X.-Z., et al. 2023, arXiv:2303.01203
Asano, K., Inoue, S., & Mészáros, P. 2009, ApJ, 699, 953
Baktash, A., Horns, D., & Meyer, M. 2022, arXiv:2210.07172

Batista, R. A. 2022, arXiv:2210.12855
Beloborodov, A. M. 2005, ApJL, 618, L13
Das, S., & Razzaque, S. 2023, A&A, 670, 12
de Ugarte Postigo, A., Izzo, L., & Pugliese, G. 2022, GCN, 32648, 1
Dermer, C. D., Chiang, J., & Mitman, K. E. 2000, ApJ, 537, 785
Dichiara, S., Gropp, J. D., Kennea, J. A., et al. 2022, ATel, 15650, 1
Finke, J. D., & Razzaque, S. 2023, ApJL, 942, 21
Finke, J. D., Razzaque, S., & Dermer, C. D. 2010, ApJ, 712, 238
Franceschini, A., Rodighiero, G., & Vaccari, M. 2008, A&A, 487, 837
Frederiks, D., Lysenko, A., Ridnaia, A., & Svinkin, D. 2022, GCN, 32668, 1
Frederiks, D., Svinkin, D., Lysenko, A. L., et al. 2023, arXiv:2302.13383
Galanti, G., Roncadelli, M., & Tavecchio, F. 2022, arXiv:2210.05659
Gallant, Y. A., & Achterberg, A. 1999, MNRAS, 305, L6
Gill, R., & Granot, J. 2022, Galax, 10, 74
Gilmore, R. C., Somerville, R. S., Primack, J. R., & Domínguez, A. 2012, MNRAS, 422, 3189
He, H.-N., Zhang, B.-B., Wang, X.-Y., Li, Z., & Mészáros, P. 2012, ApJ, 753, 178
Huang, Y., Hu, S., Chen, S., et al. 2022, GCN, 32677, 1
Inoue, S., Granot, J., O'Brien, P. T., et al. 2013, APh, 43, 252
Ioka, K., Kobayashi, S., & Zhang, B. 2005, ApJ, 631, 429
Isravel, H., Pe'er, A., & Begue, D. 2022, arXiv:2210.02363
Kakuwa, J., Murase, K., Toma, K., et al. 2012, MNRAS, 425, 514
Kimura, S. S., Murase, K., Ioka, K., et al. 2019, ApJL, 887, L16
Kobayashi, S. 2000, ApJ, 545, 807
Kumar, P., & Zhang, B. 2014, PhR, 561, 1
Li, H., & Ma, B.-Q. 2023, APh, 148, 102831
Li, T. P., & Ma, Y. Q. 1983, ApJ, 272, 317
Ma, X.-H., Bi, Y.-J., Cao, Z., et al. 2022, ChPhC, 46, 030001
MAGIC Collaboration 2019, Natur, 575, 455
MAGIC Collaboration, Veres, P., & Bhat, P. N. 2019, Natur, 575, 459
Mészáros, P. 2006, RPPh, 69, 2259
Mészáros, P., & Rees, M. J. 1994, MNRAS, 269, L41
Miceli, D., & Nava, L. 2022, Galax, 10, 66
Mirabal, N. 2023, MNRAS, 519, L85
Murase, K. 2007, PhRvD, 76, 123001
Murase, K., Dermer, C. D., Takami, H., & Migliori, G. 2012, ApJ, 749, 63
Murase, K., Ioka, K., Nagataki, S., & Nakamura, T. 2008, PhRvD, 78, 023005
Murase, K., Mukhopadhyay, M., Kheirandish, A., Kimura, S. S., & Fang, K. 2022, ApJL, 941, L10
Murase, K., Toma, K., Yamazaki, R., & Mészáros, P. 2011, ApJ, 732, 77
Murase, K., Toma, K., Yamazaki, R., Nagataki, S., & Ioka, K. 2010, MNRAS, 402, L54

Murase, K., Zhang, B., Takahashi, K., & Nagataki, S. 2009, MNRAS, 396, 1825
Nakagawa, S., Takahashi, F., Yamada, M., & Yin, W. 2023, PhLB, 839, 137824
O'Connor, B., et al. 2023, arXiv:2302.07906
Omodei, N., Bruel, P., & Bregeon, J. 2022a, GCN, 32760, 1
Omodei, N., Bruel, P., & Bregeon, J. 2022b, GCN, 32916, 1
Panaitescu, A., & Kumar, P. 2004, MNRAS, 353, 511
Particle Data Group, Zyla, P. A., Barnett, R. M., et al. 2020, PTEP, 2020, 083C01
Pillera, R., Bissaldi, E., Omodei, N., La Mura, G., & Longo, F. 2022, ATel, 15656, 1
Racusin, J. L., Karpov, S. V., Sokolowski, M., et al. 2008, Natur, 455, 183
Ren, J., Wang, Y., Zhang, L.-L., & Dai, Z.-G. 2022,
Sari, R. 1997, ApJ, 489, L37
Sari, R., & Esin, A. A. 2001, ApJ, 548, 787
Sari, R., & Piran, T. 1995, ApJL, 455, L143
Sato, Y., Murase, K., Ohira, Y., & Yamazaki, R. 2023, MNRAS, Advance Access
Sironi, L., Keshet, U., & Lemoine, M. 2015, SSRv, 191, 519
Svensson, R. 1987, MNRAS, 227, 403
Takahashi, K., Murase, K., Ichiki, K., Inoue, S., & Nagataki, S. 2008, ApJL, 687, L5
Abbasi, R., Ackermann, M., Adams, J., et al. 2023, ApJL, 946, L26
Totani, T. 1998, ApJ, 502, L13
Toma, K., Wu, X.-F., & Mészáros, P. 2011, MNRAS, 415, 1663
Troitsky, S. V. 2022, JETP Letters, 116, 767
Veres, P., Bissaldi, E., Meegan, C. & Fermi GBM Team 2022, GCN, 31816, 1
Veres, P., & Mészáros, P. 2014, ApJ, 787, 168
Vietri, M. 1996, MNRAS, 278, L1
Wang, X.-Y., Bi, X.-J., Cao, Z., et al. 2022, ChPhC, 46, 030003
Wang, X.-Y., Li, Z., & Mészáros, P. 2006, ApJL, 641, L89
Waxman, E. 1995, PhRvL, 75, 386
Waxman, E., & Bahcall, J. N. 2000, ApJ, 541, 707
Zhang, B., & Mészáros, P. 2001, ApJ, 559, 110
Zhang, B. T., Murase, K., Kimura, S. S., Horiuchi, S., & Mészáros, P. 2018, PhRvD, 97, 083010
Zhang, B. T., Murase, K., Veres, P., & Mészáros, P. 2021a, ApJ, 920, 55
Zhang, B. T., Murase, K., Yuan, C., Kimura, S. S., & Mészáros, P. 2021b, ApJL, 908, L36
Zhao, Z.-C., Zhou, Y., & Wang, S. 2023, EPJC, 83, 92
Zhu, J., & Ma, B.-Q. 2022, arXiv:2210.11376